LAWRENCE
LIVERMORE
NATIONAL
LABORATORY

LLNL-JRNL-660657

# Performance and mix measurements of indirect drive Cu doped Be implosions

D. T. Casey, T. Woods, V. A. Smalyuk, O. A. Hurricane, V. Y. Glebov, C. Stoeckl, W. Theobald, R. Wallace, A. Nikroo, C. Shuldberg, K. J. Wu, J. A. Frenje, F. Perez, O. L. Landen, B. Remington, G. Glendinning

September 18, 2014

Physical Review Letters

**Disclaimer**

This document was prepared as an account of work sponsored by an agency of the United States government. Neither the United States government nor Lawrence Livermore National Security, LLC, nor any of their employees makes any warranty, expressed or implied, or assumes any legal liability or responsibility for the accuracy, completeness, or usefulness of any information, apparatus, product, or process disclosed, or represents that its use would not infringe privately owned rights. Reference herein to any specific commercial product, process, or service by trade name, trademark, manufacturer, or otherwise does not necessarily constitute or imply its endorsement, recommendation, or favoring by the United States government or Lawrence Livermore National Security, LLC. The views and opinions of authors expressed herein do not necessarily state or reflect those of the United States government or Lawrence Livermore National Security, LLC, and shall not be used for advertising or product endorsement purposes.

LLNL-JRNL-660657

# Performance and mix measurements of indirect drive Cu doped Be implosions

D. T. Casey,[1] D. T. Woods,[1] V. A. Smalyuk,[1] O. A. Hurricane,[1] V. Y. Glebov,[2] C. Stoeckl,[2] W. Theobald,[2] R. Wallace,[1] A. Nikroo,[3] M. Schoff,[3] C. Shuldberg,[3] K. J. Wu,[1] J. A. Frenje,[4] O. L. Landen,[1] B. A. Remington,[1] and G. Glendinning[1]

1) Lawrence Livermore National Laboratory, Livermore, CA 94550
2) Laboratory for Laser Energetics, University of Rochester, Rochester, NY 14623
3) General Atomics, San Diego, CA 92121
4) Massachusetts Institute of Technology, Cambridge, MA 02139

The ablator couples energy between the driver and fusion fuel in inertial confinement fusion (ICF). Due to its low opacity, high solid density, and material properties Beryllium has long been considered an ideal ablator for ICF ignition experiments at the NIF. We report here the first indirect drive Be implosions driven with shaped laser pulses and diagnosed with fusion yield at the OMEGA laser. The results show good performance with DD neutrons yields of ~$2\times10^9$ at a convergence ratio of $R_0/R$~10 and little impact due to the growth of hydrodynamic instabilities and mix. In addition, the effect of adding an inner liner of W between the Be and DD is demonstrated.

In inertial confinement fusion (ICF) experiments, like those performed at the National Ignition Facility (NIF) [1] and the OMEGA laser facility [2], capsules of deuterium and tritium fuel are imploded to high densities and temperatures to initiate fusion burn. The indirect drive ICF concept uses a laser to irradiate a hohlraum, which produces a nearly uniform thermal x-ray drive. The x-ray drive then ablates the outer capsule material imploding the remaining cryogenically frozen DT shell-mass inward. The conditions necessary for ignition are related to a minimum requirement of the energy density delivered to the DT hotspot and the confinement time of that energy; or equivalently $P\tau$, the product of the hotspot pressure ($P$), a measure of the hotspot energy density, and the energy confinement time ($\tau$) [3]. Betti *et al.* [4] showed that $P$ is related to the implosion velocity ($v$) by balancing the hotpot internal energy to the shell kinetic energy via $2\pi PR^3 \sim \theta \frac{1}{2} M v^2$, where $R$ is the radius of the hotspot, $\theta$ is the fraction of the shell kinetic energy converted to hotspot energy, and $M$ is the mass of the shell. Note that assuming a thin shell results in $M \sim 4\pi R^2 \times \rho R$, where $\rho R$ is the areal density of the imploded shell. From Newton's law, the hotspot confinement time is related to the shell inertia like $\tau \sim \sqrt{\frac{M}{4\pi PR}}$. Combining these expressions show that $P\tau \propto v \times \rho R$ [4]. This means that a successful ignition experiment must achieve high $v$ and high $\rho R$. In the attempt to achieve these conditions, several ablator materials have been considered, i.e. plastic (CH), high density carbon (HDC), and beryllium. The choice of ablator material has important consequences for the implosion hydrodynamics. For example, the mass ablation rate ($\dot{m}$) can be quite different for different materials. Olson *et al.* [5] measured $\dot{m}$ (in mg/cm$^2$/ns) experimentally and found it to be 0.75 $T_r^3$ for Be (with and without 1% Cu dopant), 0.50 $T_r^3$ for HDC, and 0.35 $T_r^3$ for CH (0.6% Ge dopant), where $T_r$ is the drive radiation temperature in units of hundreds of eV (or heV). Because the ablation velocity is $V_a = \dot{m}/\rho$ , where $\rho$ is the ablator density, Be has the highest $V_a$ for the same inflight $\rho$. Also, Lindl *et al.* have shown that the maximum implosion velocity ($v_{imp}$) depends on the $V_a$ and the inflight aspect ratio ($R/\Delta R$) like $v_{imp} \sim 0.56 \frac{R}{\Delta R} V_a$ [6]. This means that, in principle, Be can achieve higher implosion velocities or operate at lower $R/\Delta R$ for a fixed driver energy. Simakov *et al.* show that the potential benefits of Be target designs still exist even with Cu-doped Be shells currently being considered for ignition experiments [7]. Wilson et al. [8] summarized many of the additional mechanical and hydrodynamic advantages of Be, such as high initial density, high tensile strength, and high thermal conductivity. The higher $V_a$ also results in less predicted ablation front instability growth, while designs can also operate at higher remaining mass and lower $R/\Delta R$ for the same implosion velocity. However, Be ablators pose many substantial challenges, particularly in target fabrication [9, 10] and Be handling, as well as inhomogeneities that may seed instability growth and mix of ablator material into the hotspot, engineering issues that may negate the more basic plasma physics advantages. Because of these challenges most NIF experiments to date have been performed with CH [11, 12] and HDC [13].

The basic x-ray ablation properties of Be have been studied in mass ablation rate measurements [5], Rayleigh-Taylor growth experiments with planar foils [14-16], and convergent ablator shell-trajectory experiments [17]. However, indirect drive experiments using fusion yield to diagnose implosion performance have not yet been performed. Such experiments are an important step forward since inhomogeneities in Be crystal structure are of particularly serious concern and may cause instability growth and mix that will harm overall implosion performance. In addition, the presence of Cu dopant may introduce additional inhomogeneities that could seed instability growth. The results described herein were obtained from indirect drive experiments driven with a two-shock shaped radiation drive and show excellent overall performance. Furthermore, they show the resulting mix of the Cu-doped Be into the hotspot has a negligible impact on the yield at a convergence ratio (initial outer radius / final hotspot radius) of ~10. These results bolster ongoing efforts [7, 18] to develop a Be ignition platform at the NIF. Furthermore, this platform utilized some targets with a thin W tracer layer which provided a valuable test of mix calculations.

The experimental configuration is illustrated in Figure 1. The laser pulse shape (shown in Figure 1a) is a 2.5 ns long pulse with a ~2.5 TW foot and a ~20 TW main drive delivered across 40 OMEGA laser beams similar to Ref. [19]. The capsules (details shown in Figure 1b) were 600 μm diameter and 30 μm thick Be shells and were filled with deuterium gas (with trace 0.02 atm of Kr used to measure the capsule leak rate via x-ray fluorescence). The Be capsules were made by coating Be onto a spherical mandrel. The inner 7.5 μm of Be was doped with 4% Cu before removal of the mandrel by pyrolysis to be as relevant as possible to the current Be designs [7, 18] and to provide radiographic contrast. After pyrolysis, the Cu dopant diffused into the undoped Be bringing the maximum Cu concentration to

2.5% with a decreasing linear radial gradient toward the outer radius of the capsule. Cross-sectional scanning-electron microscope images of the Be capsules before and after pyrolysis are shown in Figure 2a and Figure 2b, respectively. Figure 2c shows the dopant concentration plotted as a function of radius before and after pyrolysis. Figure 2c also shows the amount of trapped Ar gas impurity in the Be resulting from the sputter coating process. Additionally, several targets included thin 0.2 µm thick W layers on the inner capsule surface to provide radiographic contrast and to serve as a gas/shell mix diagnostic (described in detail later). The capsules were driven by 1.6 mm diameter by 2.1 mm long Au hohlraums (50 µm thick) with a 0.8 mm laser entrance hole (LEH).

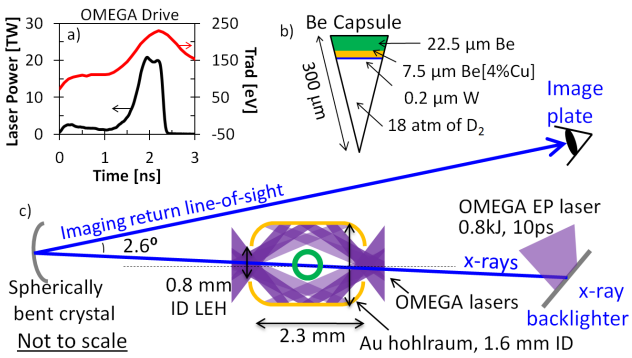


Figure 1: Overview of the experimental configuration. a) Shaped laser pulse shape (black curve) used to produce the hohlraum drive (Omega shape LA232301) and radiation temperature (Trad) obtained using the DANTE [20, 21] diagnostic (red curve). b) Schematic of the $D_2$ gas filled Be capsule. Half of capsules had a 0.2µm W inner layer. c) The hohlraum and capsule are backlit using a Cu k-α x-rays produced using the OMEGA EP laser with a 0.8kJ, 10 ps, laser pulse. The backlighter x-rays are recorded on an image plate using a spherical crystal imager, which provides a very narrow bandpass image (~8 eV).

To observe the capsule inflight, the target was backlit with Cu k-α x-rays produced by the OMEGA EP laser [22, 23] delivering a 0.8 kJ, 10 ps, laser pulse onto a 1 $mm^2$ and 25 µm thick Cu foil. The overall geometry is illustrated in Figure 1c. The backlighter x-rays are recorded with a spherical crystal imager (SCI) described in detail in Ref. [24], which provides a very narrow bandpass image (~8 eV) at 8.05 keV. The SCI uses a quartz crystal with an 88.7° Bragg angle and is 26.7 cm from the target and 393 cm to an image plate detector establishing a magnification of 14.7 [25]. The resolution was determined to be ~10 µm using a Au grid with 37 µm hole and a 25 µm bar width.

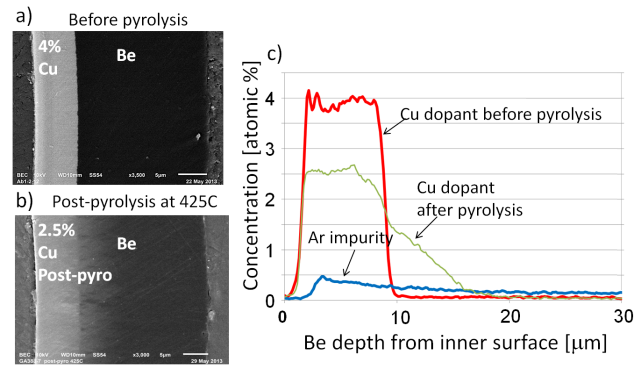


Figure 2: a) A cross-sectional image of the Be capsule before the mandrel is removed by pyrolysis. b) A cross-sectional image of the Be capsule after the mandrel is removed. c) Profiles of Cu dopant before and after pyrolysis and of the reminant Ar from the coating process.

The SCI view of the capsule through the hohlraum LEH is illustrated in Figure 3a (modelled by VISRAD [26]). The hohlraum axis is tilted 3° from the SCI axis as shown in Figure 1c. A 10 ps (duration of the EP backlighter) snapshot image of the imploding capsule, backlit near peak drive at 2.17 ns with respect to the start of the laser drive is shown Figure 3b. The backlighter x-rays are seen through the hohlraum LEHs. The in-flight imploding capsule shell at a convergence ratio of $R_0/R=1.5$ is clearly seen in the radiograph. Most of the observed contrast is from the thin W layer at the capsule inner surface. A self-emission hotspot is evident in the center of the radiograph from the capsule compression. This later-time emission is apparent because, although the backlighter was fired at 2.17 ns for only 10 ps, the image plate is a time-integrated detector. Figure 3c shows a radiograph backlit near the end of the drive at 2.43 ns showing the inflight shell at a $R_0/R=2.1$.

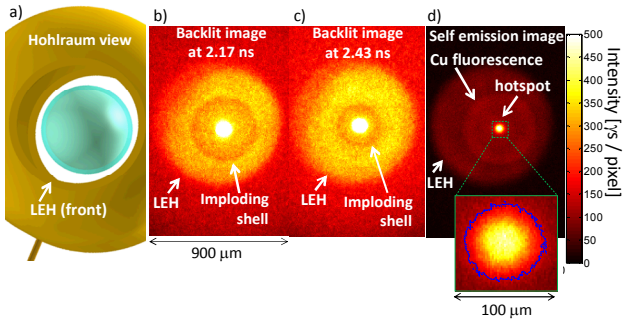


Figure 3: a) View of the capsule with the spherical crystal imager, which is 3° off the hohlraum polar axis. b) Backlit image of the imploding shell at 2.17 ns using a 10 ps OMEGA EP driven Cu kα backlighter. The central feature is the hotspot self-emission. c) Backlit image of the imploding shell at 2.43ns. d) Time-integrated self-emission image of the capsule. The hotspot is blown up in the lower panel. A 17% intensity contour is illustrated in blue corresponding to a mean hotpot radius of 38 µm. Note that panels b, c, and d are on the same color scale but that panel d shows a target without W, which is not as bright as the targets with W, described in more detail in the text. Note also that the color scale for panels b and c are saturated to emphasize the imploding shell (making the apparently hotspot size appear larger by emphasizing lower contours) however the image plate data is not saturated.

The SCI was also used to image the hot-spot self-emission at peak compression without the EP backlighter. Figure 3d shows a self-emission radiograph. The hohlraum outside the LEH casts a distinct shadow. A Cu K-α fluorescent ring is observed from pumping of the Cu dopant in the Be shell by hot-spot continuum x-rays at bangtime. An expanded view of the time-integrated hotspot image is shown in the lower panel. The 17% intensity contour is shown in blue showing a round hotspot with a mean radius of 38 µm from a polar view.

Two-dimensional simulations were performed using the radiation-hydrodynamics code LASNEX [29]. The calculations included the hohlraum and laser energy deposition using a laser propagation model. All laser power time histories were used as shot, i.e. no adjustment was made to the laser energies to match any of our observations. The impact of turbulence was assessed using a k-epsilon turbulence model [30], where the mix parameters have been validated against Z-pinch experiments.

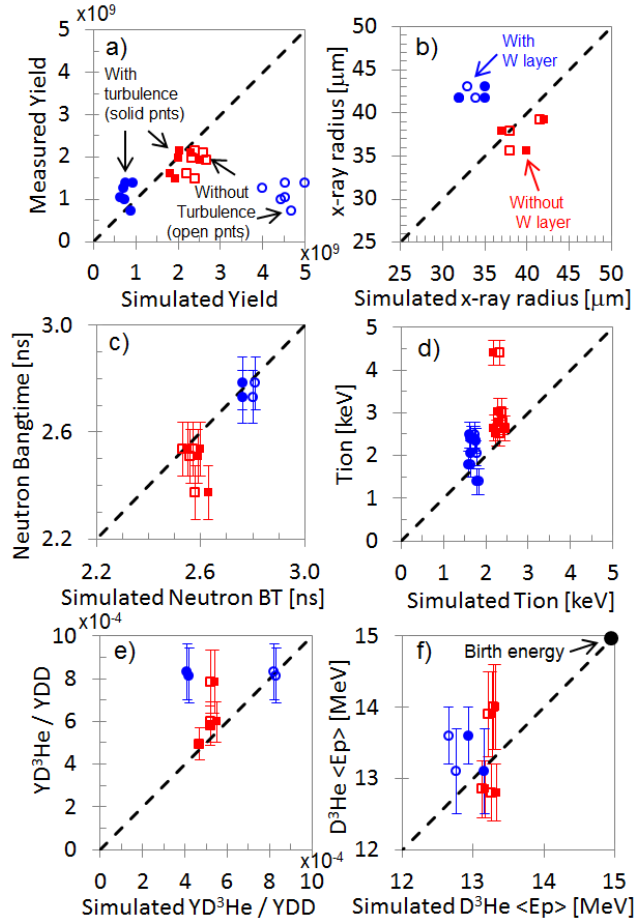


Figure 4: Performance observations plotted as a function of simulated observable. In all of the panels, blue points represent targets with a 0.2 µm thick W tracer layer on the gas/shell interface, while red squares are without. On the abscissa, solid symbols show simulations that include turbulent mix, while open symbols show simulations without. a) Measured DD neutron yield from the OMEGA nTOF diagnostic suite [27] as a function of simulated yield. Note the experimental uncertainties are suppressed for clarity and are of order the symbol size. b) Hot spot radius measured from the x-ray self-emission radiographs with the SCI. Note the experimental uncertainties are suppressed for clarity and are of order the symbol size. c) DD Neutron bangtime measured using the neutron bangtime detector. d) Burn weighted ion temperature measured using the Doppler broadened 2.45 MeV DD neutron peak observed with the nTOF diagnostics. e) $D^3He$ proton yield, collected with WRFs over three lines of sight, normalized by the DD neutron yield, which is sensitive to the fuel areal density [28]. f) Secondary $D^3He$ proton energy measured with three WRFs at different lines of sight, which is sensitive to the total fuel and shell areal densities.

The measured DD neutron yield, obtained using the OMEGA nTOF diagnostic suite [27], is shown in Figure 4a as a function of the simulated yield. The red squares are implosions without the 0.2 µm W tracer layer (illustrated in Figure 1b), whereas the blue circles are implosions with the 0.2 µm W tracer. The shots with W inner layers produced less DD neutron yield indicating that W mixes into the hotspot and degrades yield by about a factor of two. Interestingly, the simulations without including turbulent mix predict higher yield with the W tracer due to a significantly higher predicted compression. However,

including the effects of mix brings the simulated yields much closer to experiment due to enhanced radiative cooling during the high compression phase that effectively quenches the DD burn similar to observations in other experiments [31]. These results show that the W targets are quite sensitive to gas/shell mix and provide a useful test of the mix model. The simulations with mix predict that it has only a small impact for the Be targets without W, when compared to simulations without mix. The hotspot radii are plotted in Figure 4b, determined from self-emission radiographs like shown in Figure 3d. Self-emission images were obtained both with and without the W tracer layer on shots without the EP backlighter and used to measure the hotspot radius defined as the radius of the 17% intensity contour. Implosions with the W tracer layer are larger by ~15%, an effect not expected or captured by simulation. This may be due to an apparent increase in radius from multiple localized W bright-spots due to breakup of the W-layer convolved with the imaging system resolution or that targets with W do not reach as high a compression as those without. Future experiments will be proposed with time resolved x-ray framing-camera measurements with higher spatial resolution to investigate this issue. The x-ray brightness inferred from the self-emission radiographs showed that targets with W were 6 times brighter at 8 keV then the targets without W. The radial dependence of the x-ray emission is another indicator of turbulent behavior. Simulations without turbulence show evidence of a bright annulus of emission at around 20 microns radius with a slightly depressed core emission, indicative of an intact W liner. By contrast, simulations including turbulence show that at neutron bangtime the W remains on the outside of the core but continues subsequently mixing inward producing a centrally peaked time-integrated x-ray emission, in agreement with the experimental results, as the predicted peak x-ray emission occurs after peak neutron emission while the W mix into the core becomes more substantial. Figure 4c shows the measured neutron burn weighted bangtime, observed using the neutron bangtime diagnostics. The targets with the W tracer layer had a somewhat delayed bangtime, principally due to the additional payload mass from the very high density W slowing the implosion velocity. Simulations predict that bangtime of these experiments is relatively insensitive to mix. Interestingly, the shot without W with the highest ion temperature (highest solid and open points in Figure 4b) also has the earliest bangtime (Figure 4c) and the lowest DD yield (Figure 4a). The DD burn weighted ion temperature is shown in Figure 4d, measured using the Doppler broadened neutron spectrum observed with nTOF detectors. The targets with W tracer layer are ~30% cooler than the targets without due to the slightly heavier shell slowing the implosion velocity. Additionally, simulations predict a weak dependence of ion temperature with and without W-mix because W-mix is predicted to be localized at the gas/shell interface rather than the central hotter part of the core at the time of neutron production. Secondary $D^3He$ protons were also collected using wedge range filter (WRF) spectrometers [28], fielded over three lines of sight (TIM 1, 2, and 5). Figure 4e shows the measured secondary $D^3He$ proton yield, which is related to deuterium ρR compared to simulation. The targets without W are in relatively good agreement with simulation but targets with W are under predicted, possibly indicating an issue with the transport of $^3He$ ions in the presence of W mix, the temperature of the unburning mix-region, or the calculated hotspot compression. Figure 4f shows the average $D^3He$ proton energy which is related to the total ρR [28]. The total areal density inferred experimentally from the $D^3He$ proton data averaged over four implosions without the W tracer layer is 66±10 mg/cm$^2$, while the total areal density averaged over the implosions with W is 75±16 mg/cm$^2$, essentially in agreement within the respective uncertainties indicating that because of mix implosions with W reach approximately the same compression as those without (within the uncertainty).

The radial transmission profiles of the radiographs taken with the SCI are shown in Figure 5a. The profile shapes are due both to a projection of a 3d spherical shell onto a 2d image plane and the convolution with the instrument resolution. The measured and simulated minimum radius of transmission versus time (including the instrument resolution) is shown in Figure 5b. Agreement within ± 100 ps is observed, which is consistent with the bangtime comparison. Figure 5b also shows simulations that including turbulence, which show minimal effect on the overall shell trajectory.

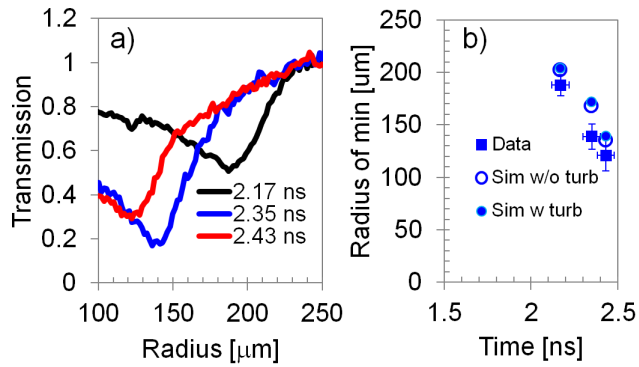


Figure 5: a) Transmission profiles produced from radiographs of the inflight shell. b) Measured (square) radius of minimum transmission as a function of time compared with simulations (open circles) and simulations including mix (closed circles).

These Be implosions were comparable to similar CH shell implosions using a similar hohlraum and laser drive [19], which showed DD neutron yields of $1.5\times10^9$, ion temperatures of 2.8 keV, and neutron bangtimes of 2.4 ns. The yield-over-simulated (YOS) for the Be targets (without the W tracer layer) is 80%, as compared to CH at ~70% [19].

The data reported here show that indirectly driven Be implosions are well reproduced by simulations at a capsule convergence ratio of ~10. The basic ablation properties of Be [5, 8], such as the high ablation velocity, can result in higher velocity and improved stability in simulated ignition designs when compared to CH or HDC designs [7, 18]. It is possible that at higher convergence, in-homogeneities, sputter material impurities, and dopant non-uniformity may seed unstable growth that could compromise performance. There may also be issues predicting the basic ablation properties of Be and Cu-doped Be such as equation-of-state, opacity, or thermal conductivity. However, at least at a convergence ratio of ~10 these issues do not seem to be significant. This work strongly supports the ongoing efforts to test Be at the more virulent conditions of high convergence at NIF [7, 18].

This work also clearly shows that metals layers on the gas/shell interface are unstable (unsurprisingly) and can mix into the hotspot degrading the performance when compared to clean predictions. There have been suggestions to use the predicted recompression from metal layers to increase overall target performance. However, the effects of mix must be carefully considered first and are likely to significantly degrade the promise of such concepts.

The authors thank the OMEGA and OMEGA-EP scientific and operations staff who supported this work. Helpful conversations with G. Zimmerman, J. Harte, D. Klem, F. Perez, H. Scott, and D. Wilson are also gratefully acknowledged. We also thank M. May for providing the DANTE data analysis. This work was performed under the auspices of the U.S. Department of Energy by Lawrence Livermore National Laboratory under Contract DE-AC52-07NA27344.

## References

[1] E. I. Moses, Journal of Physics: Conference Series **112**, 012003 (2008).
[2] T. R. Boehly *et al.*, Optics Communications **133**, 495 (1997).
[3] J. P. Freidberg, *Plasma physics and fusion energy* (Cambridge University Press, Cambridge, 2007).
[4] R. Betti *et al.*, Physics of Plasmas **17**, 058102 (2010).
[5] R. E. Olson *et al.*, Physics of Plasmas **18**, 032706 (2011).
[6] J. D. Lindl *et al.*, Physics of Plasmas **11**, 339 (2004).
[7] A. N. Simakov *et al.*, Physics of Plasmas **21**, 022701 (2014).
[8] D. C. Wilson *et al.*, Physics of Plasmas **5**, 1953 (1998).
[9] A. Nikroo *et al.*, Physics of Plasmas **13**, 056302 (2006).
[10] A. Nobile *et al.*, Laser and Particle Beams **24**, 567 (2006).
[11] M. J. Edwards *et al.*, Physics of Plasmas **20**, 070501 (2013).
[12] O. A. Hurricane *et al.*, Nature **506**, 343 (2014).
[13] A. J. MacKinnon *et al.*, Physics of Plasmas (1994-present) **21** (2014).
[14] E. N. Loomis *et al.*, Physics of Plasmas (1994-present) **17** (2010).
[15] M. M. Marinak *et al.*, Physics of Plasmas (1994-present) **9**, 3567 (2002).
[16] J. A. Cobble *et al.*, Physics of Plasmas (1994-present) **13** (2006).
[17] D. G. Hicks *et al.*, Physics of Plasmas (1994-present) **17** (2010).
[18] S. A. Yi *et al.*, Physics of Plasmas **21**, 092701 (2014).
[19] J. S. Ross *et al.*, Sci. Rep. **3** (2013).
[20] H. N. Kornblum, R. L. Kauffman, and J. A. Smith, Review of Scientific Instruments **57**, 2179 (1986).
[21] M. J. May *et al.*, Review of Scientific Instruments **83**, 10E117 (2012).
[22] C. Stoeckl *et al.*, Fusion Sci. Technol. **49**, 367 (2006).
[23] L. J. Waxer *et al.*, Opt. Photon. News **16**, 30 (2005).
[24] C. Stoeckl *et al.*, Review of Scientific Instruments **83** (2012).
[25] D. B. Sinars *et al.*, Appl. Opt. **42**, 4059 (2003).
[26] MacFarlane J J 2003 J. Quant. Spectrosc. Radiat. Transfer 81 287.
[27] V. Y. Glebov *et al.*, Review of Scientific Instruments **81**, 10D325 (2010).
[28] F. H. Seguin *et al.*, Review of Scientific Instruments **74**, 975 (2003).
[29] G. Zimmermann, and W. Kruer, Comments on Plasma Physics and Controlled Fusion **2**, 51 (1975).
[30] J.H. Hammer and G.B. Zimmerman, "Magnetohydrodynamic turbulence model", Bull. of the APS Div. of Plasma Phys. 47th Annual Meeting, C03.00010 (2005). Op. cit. LLNL Internal Report UCRL-ABS-213676.
[31] A. R. Miles *et al.*, Physics of Plasmas (1994-present) **19**, 072702 (2012).